Journal of Materials Chemistry A

Computational Prediction of Solvation Structure in Calcium Battery Electrolytes

Journal:	*Journal of Materials Chemistry A*
Manuscript ID	TA-ART-09-2024-006675.R1
Article Type:	Paper
Date Submitted by the Author:	29-Oct-2024
Complete List of Authors:	Jeong, Heonjae; Gachon University, Electronic Engineering Wang, Haimeng; Argonne National Laboratory, Cheng, Lei; Oak Ridge National Laboratory, Energy Storage Group

Computational Prediction of Solvation Structure in Calcium Battery Electrolytes

Heonjae Jeong[a,b,c*], Haimeng Wang[a,b], Lei Cheng[a,b]

[a]*The Joint Center for Energy Storage Research (JCESR), Argonne National Laboratory, Lemont, Illinois 60439, United States*

[b]*Materials Science Division, Argonne National Laboratory, Lemont, Illinois 60439, United States*

[c]*Department of Electronic Engineering*, *Gachon University, 1342 Seongnam-daero, Seongnam, Gyeonggi 13120, South Korea*

*hjeong@gachon.ac.kr

Keywords: calcium battery electrolytes, solvation structure, ab initio molecular dynamics, density functional theory, machine learning force filed

Abstract

Calcium ion battery is emerging as a key focus in the pursuit of alternatives to lithium ion. However, a crucial gap remains in understanding how different electrolyte species influence their solvation structures. In this study, we demonstrate a comprehensive predictive approach that integrates ab initio calculations and machine learning force fields (MLFF) to address this challenge. Using ab initio molecular dynamics (AIMD) simulations, we accurately predict the solvation structures within the first solvation shell, while also evaluating their reductive and oxidative stability through frontier orbital analysis. This analysis compares both implicit and explicit electrolyte conditions. To further elucidate these structures, we calculate and visualize their formation free energies using density functional theory (DFT), combined with heat map analysis. Additionally, MLFF simulations extend our predictions to nanosecond-scale trajectories, surpassing the limitations of picosecond-scale AIMD. The predicted solvated structures show strong agreement with both AIMD and DFT results, demonstrating the robustness of our approach. Thus, by leveraging these comprehensive methods, we provide a more reliable framework for predicting solvation structures in calcium ion and other battery electrolytes.

Introduction

Calcium (Ca) ion batteries are being actively studied as the next generation of multivalent ion batteries, following magnesium (Mg) ion batteries, because they offer higher voltage and greater energy density compared to lithium (Li) ion batteries.[1] However, the slower ion diffusivity in the Ca electrolyte systems is unavoidable due to the larger ion size and doubly positive charge of the Ca cation. Additionally, the nature of the solid electrolyte interphase (SEI) of Ca system differs from that of the Mg and Li systems. These challenges have driven the investigation of high-performance chemically stable electrolytes.[2–4]

Over the past five years, various Ca battery electrolytes have been explored both theoretically [5–8] and experimentally[9–11] by benchmarking against Li and Mg battery electrolytes that use anions like $TFSI^-$, BF_4^-, PF_6^-, $CB_{11}H_{12}^-$, BH_4^-, and $B(HFIP)_4^-$. Despite promising advances in synthesizing Ca salts, directly applying Li and Mg benchmarks to Ca battery systems has been proven difficult.[12] Therefore, computational modeling and simulations are particularly valuable for developing Ca battery electrolytes.

Studies on Ca battery electrolytes seek to find better options by analyzing the intrinsic stability of electrolyte molecules[13,14] and their electrochemical stability at the electrolyte-electrode interface, including interfaces with Ca metal, [13–16] graphene (graphite), [17,18] and oxide.[19] There is limited research on the solvation structure of Ca battery electrolytes, and studies involving new material combinations are even rarer. Experimentally, manipulating solvation structures using different anions and solvents has been used to predict their solvation structures and potential SEI products. However, only a few studies have been reported, such as $Ca(TFSI)_2$ with G1, G2, or G3,[10] $Ca(BH_4)_2$:THF, [20] $Ca(BH_4)_2$:THF/G1(or $Ca(BH_4)_2$:THF/G2)[21] $Ca(CB_{11}H_{12})_2$:THF, [20] $Ca(BF_4)_2$:EC/DEC/DMC/EMC [22], and $Ca(B(HFIP)_4)_2$:G1.[23] From a computational standpoint, no single methodology is universally optimal. Therefore, it is important to validate whether consistent results can be predicted using different approaches to complement each other's limitations.

In this study, we report two major findings regarding the solvation structures of Ca battery electrolytes using various computational methods. First, we comprehensively predict the solvation structures of Ca battery electrolytes by combining various salts and solvents, including both relatively recent salts and the salts benchmarked from Li and Mg ions. For recent Ca salts with alkoxy anions, they have been extensively studied in a decade due to their chloride-free and weakly coordinated nature. [13,23,24] We demonstrate a straightforward method to predict solvation preferences using heat map analysis from density functional theory (DFT) calculations. Second, we verifiy whether consistent solvation results could be predicted for specific electrolyte molecules using various analyses based on first-principles calculations. Ab initio molecular dynamics (AIMD) calculations are particularly useful for predicting the solvation of new electrolyte structures. However, AIMD simulations are computationally expensive and slow, making them suitable for accurate initial solvation reaction models but less reliable for predicting equilibrium states. To address these issues, we use machine learning force fields (MLFF) to model and predict the solvation structure of $Ca(TFSI)_2$:G1 electrolytes, overcoming the timescale limitations of AIMD trajectories. We confirm the similarity between AIMD and MLFF calculation results, providing valuable insights into the future direction of computational approaches. Furthermore, these results align well with predictions from the heat map analysis of DFT results. This comprehensive computational study serves as a robust example of predicting solvation structures in Ca battery electrolytes by combining DFT, AIMD, and MLFF approaches. It also provides useful guidance for future experiments based on these plausible solvation structures.

Methods

1. Electrolyte Design

Based on several previous studies on multivalent ion batteries, [10,24,25] we set a typical solvation condition with a molar concentration of 0.5 M and a density of 1.0 g/ml for a parallel comparison, as we lacked experimental reference conditions for different combinations of solvents and anions. To establish the initial solvation structure, we adjusted the simulation box size in a cubic shape, and used the Packmol package to wrap Ca salt species and solvents.[26] To avoid the artifact introduced by limited simulation trajectories and the structure getting trapped in a local minimum, we started the AIMD simulations with three different initial solvation structures, solvent-separated ion pair (SSIP), contact ion pair-1 (Ca cation bonded to one anion, CIP-A1, and the other anion was far from the Ca cation), and contact ion pair-2 (Ca cation bonded to two anions, CIP-A2). The modeling variables of Ca battery electrolyte species are anions and solvents. The lists of solvents are monoglyme (dimethoxyethane (DME) or G1) and ethylene carbonate (EC). G1 is ether-based solvent and has linear shape, whereas the EC is the carbonate-based solvent and possess a cyclic shape. The lists of anions are boron and aluminum alkoxylates in conjunction with other common anions, such as bis-(trifluoromethanesulfonyl)imide ($TFSI^-$), hexafluorophosphate

(PF_6^-), and carba-closo-dodecarborate ($CB_{11}H_{12}^-$), and tetraphenylborate (BPh_4^-). Building upon the intrinsic chemical stability result elsewhere, [13] for boron fluorinated alkoxy anions ($B(ligand)_4^-$ or $B(ligand)_2^-$), we considered monodentate trifluoro-isopropyl ligand (TFIP, $OC(H)(CF_3)(CH_3)$), monodentate hexafluoro-isopropyl ligand (HFIP, $OC(H)(CF_3)_2$)), monodentate trifluoro-isopropyl ligand (TFIP, $OC(H)(CF_3)(CH_3)$), monodentate hexafluoro-isopropyl ligand (HFIP, $OC(H)(CF_3)_2$)), and perfluorinated pinacolato ligand (PIN, $O_2C_2(CF_3)_4$). For aluminum fluorinated alkoxy anions ($Al(ligand)_4^-$), we considered monodentate trifluoro-tert-butyl ligand (TFTB, $OC(CF_3)(CH_3)_2$), hexafluoro-tert-butyl ligand (HFTB, $OC(CF_3)_2(CH_3)$), and perfluoro-tert-butyl ligand ($PFTB^-$, $OC(CF_3)_3$)).

2. First-Principles Calculations: DFT and AIMD

We studied a solvation structure of Ca battery electrolytes using first-principles calculations. In the first-principles calculations, DFT and AIMD were used to predict the stable geometries and their frontier orbital states of Ca battery electrolyte molecules.

To run DFT calculation, we used Gaussian 16 [27] with a basis Becke, 3-parameter, Lee-Yang-Parr (B3LYP) functional and a basis set of 6-311++G(d,p). [28–30] The DFT calculations were performed in the presence of an implicit organic solvents. For implicit solvation environment, we adjusted the dielectric constant using the SMD model with glyme (G1, ε_r= 7.2), diglyme (G2, ε_r= 7.23), ethylene carbonate (EC, ε_r= 89.6), and tetrahydrofuran (THF, ε_r= 7.42), respectively. **Figure S1** schematizes a combination of solvents and anions with molecular structures in a tabulate form. G1 and G2 represent the glyme organic solvent and EC and THF represent the heterocyclic ether.

To run AIMD simulation, we used Vienna *Ab Initio* Simulation Package (VASP). [31,32] We set a temperature of 298 K and the Nosé-Hoover thermostat and canonical ensemble (NVT) simulations. Perdew-Burke-Ernzerhof (PBE) [33] generalized gradient approximation (GGA) exchange-correlation functional and the projector augmented wave (PAW) [34] pseudopotentials were used. We set the plane wave cutoff energy of 460 eV. We set Monkhorst-Pack *k*-point sampling at Γ-point due to the high computational demands. For all configurations, all atoms were relaxed until the force on each atom is smaller than 0.01 eV/Å.

We counted the AIMD trajectories for 10-15 ps despite the high demands of calculation expense. We further analyzed the frontier orbital energy levels (highest occupied molecular orbital

(HOMO) and lowest unoccupied molecular orbital (LUMO)) using the last 2-5 ps trajectories of AIMD.

3. Machine Learning Force Fields

AIMD provides high computational accuracy but is limited by short simulation timescales and high computational costs. In contrast, classical molecular dynamics (MD) allows for longer simulation timescales with lower computational costs, but this is accompanied by less accurate force field representations. As an alternative, a MLFF can be trained based on the AIMD trajectories, which can then be applied in MD simulations to explore solvation structures.

Based on this perspective, we used a MLFF to predict the solvation structures over the extended timescale of AIMD simulations. The whole procedure is consisted of three parts: the data collection part, the training part, and the MD simulation part. The architecture of the MLFF in this work is the Deep Potential Smooth Edition (DeepPot-SE) implemented in the DeePMD-kit package. [35] The DPGEN package [36] was used in the data collection part, and MD simulations were done with a customized version of LAMMPS [37] with the DeePMD-kit plug-in. Due to the high computational expense, this procedure was only performed for the system of 0.5 M $Ca(TFSI)_2$:G1.

As mentioned above, the DPGEN package was used to obtain a higher volume of the training data for the MLFF. Based on the AIMD simulation results as the initial datasets, an active learning procedure was performed with the DPGEN package. This is important because that more data was required to train a stable and accurate MLFF due to the complexity of the electrolyte systems and the limited timescale of AIMD simulations. In the DPGEN package, the data was gathered with several iterations and each iteration consists of three steps: training, exploration, and first-principles calculations (or labeling). This workflow is schematized in **Figure 1**. In the training step and exploration step, a large portion of configurations were generated and only a part of them were selected to be labeled based on the active learning algorithm. Then for the first-principles calculations step, we used VASP to perform the single-point calculations for the selected configurations. The atomic forces and potential energies were calculated for each configuration and the results were added to the training datasets. We iterated a cycle of training, exploration, and first-principles calculations until the exploration accuracy converges below the set value. A total of 6 iterations were completed and 34496 more data points were collected in this process. The iterative process was stopped when there was less than 5% of the configurations labelled in the last iteration. More details about the DPGEN active learning process can be found in the reference. 36

In the force field training part, the MLFF was trained with the DeePMD-kit based on the atomic forces and the potential energies from the AIMD trajectories (35000 configurations) and data generated with the DPGEN package (34496 configurations). The number of neurons was 25, 50, and 100 for the embedded neural network and 240, 240, and 240 for the fitting neural network. The batch size was 8 and the total number of batches was 150000 for the training procedure.

After the MLFF was obtained, it was used to run MD simulations. The MD simulations with the MLFF were started with 3 different initial structures (SSIP, CIP-A1, and CIP-A2), and 3 parallel simulations were run for each different initial structure. The length of the simulation is 1 ns for each simulation, and the timestep was 0.5 fs.

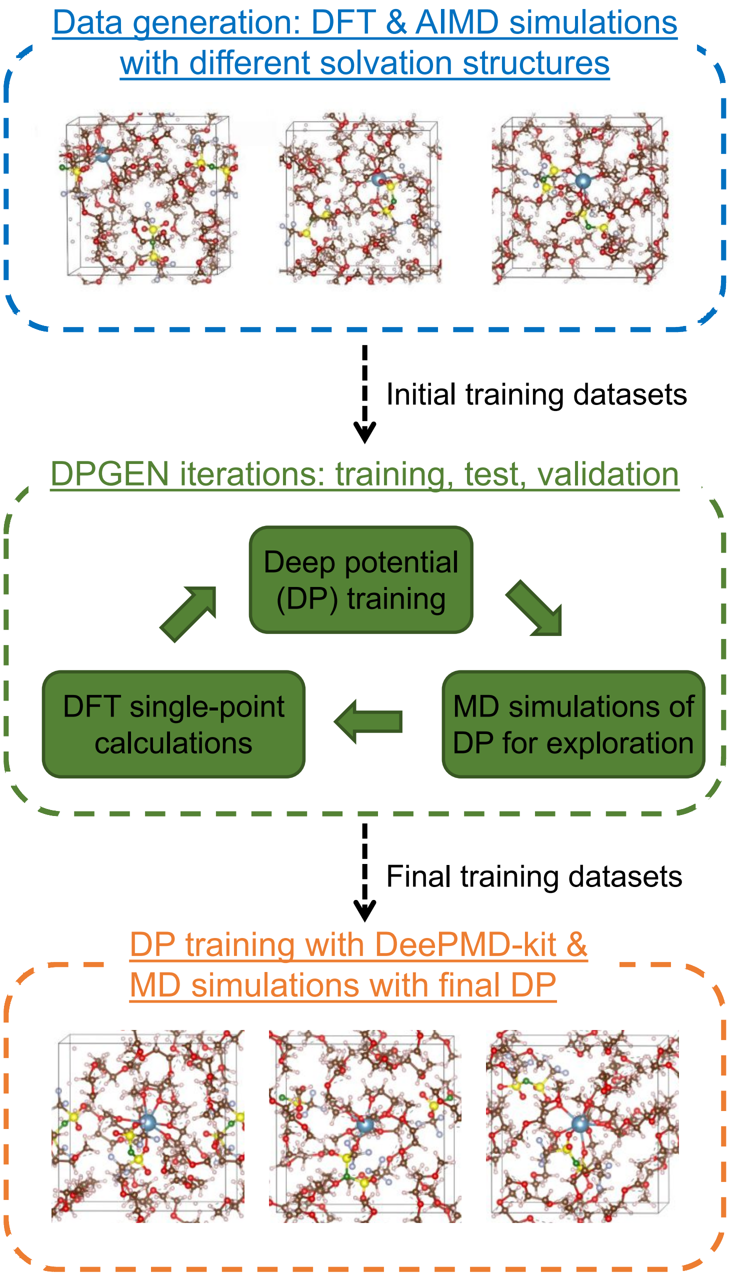

Figure 1. The workflow to predict the solvation structures using MLFF.

4. Formation Free Energy Calculations

We computed the formation free energy (ΔG) between SSIP and CIPs (CIP-A1 and CIP-A2) at 298 K and the results were visualized through heat map plots (a data visualization method that encodes the magnitude of formation energies within a dataset through variations in color). Equation (1) illustrates the formation free energy required to form SSIP from CIP-A2, and it is given by:

$$G(\mathrm{Ca(anion)_2}) + G(\mathrm{n(solvent)}) \xrightarrow{\Delta G} G(\mathrm{Ca(solvent)_n^{2+}}) + G(\mathrm{2(anion)^-}) \quad (1).$$

Here, $G(\mathrm{Ca(anion)_2})$ represents the free energy of the Ca cation with two anions (CIP-A2), $G(\mathrm{n(solvent)})$ is the free energy of the solvent, which depends on the number of molecules (n), $G(\mathrm{Ca(solvent)_n^{2+}})$ is the free energy of the Ca solvent solvated by a specific number of solvent molecules (n), and $G(\mathrm{2(anion)^-})$ is the free energy of two anions. For the case of Ca cation with one anion (CIP-A1), we employed Equation (2) to compute the formation free energy (ΔG):

$$G(\mathrm{Ca(anion)^+}) + G(\mathrm{n(solvent)}) \xrightarrow{\Delta G} G(\mathrm{Ca(solvent)_n^{2+}}) + G(\mathrm{(anion)^-}) \quad (2).$$

Here, $G(\mathrm{Ca(anion)^+})$ represents the free energy of the Ca cation with one anion, and $\mathrm{G((anion)^-)}$ is the free energy of one anion. If ΔG is positive, CIP formation is favored; otherwise, SSIP is favored. For the comparison of CIP-A1 and CIP-A2, we utilized Equation (3) to calculate the formation free energy (ΔG):

$$G(\mathrm{Ca(anion)^+}) + G(\mathrm{(anion)^-}) \xrightarrow{\Delta G} G(\mathrm{Ca(anion)_2}) \quad (3).$$

In this equation, $G(\mathrm{Ca(anion)^+})$ is the free energy of the Ca cation with one anion (CIP-A1), $G(\mathrm{(anion)^-})$ is the free energy of one anion, and $G(\mathrm{Ca(anion)_2})$ is the free energy of the Ca cation with two anions (CIP-A2). If ΔG is positive, CIP-A1 formation is favored; otherwise, CIP-A2 is favored.

Results

1. Solvation Structure Predicted from AIMD

In this section, we focus on the solvation structures predicted by AIMD. For anions, we present the solvation structure of fluorinated alkoxy anions and compare it with other anions. For solvents, we examine the solvation structure in G1 (an ether) and EC (a cyclic carbonate ester). The results of the solvation structure predicted by AIMD are presented in **Tables 1-3**.

	Anions											
	Fluorinated Alkoxy Anions								**Other Anions**			
	Borates			**Aluminates**								
Solvents	**$B(TFIP)_4$**	**$B(HFIP)_4$**	**$B(PIN)_2$**	**$Al(TFIP)_4$**	**$Al(HFIP)_4$**	**$Al(TFTB)_4$**	**$Al(HFTB)_4$**	**$Al(PFTB)_4$**	**TFSI**	**PF_6**	**$CB_{11}H_{12}$**	**BPh_4**
G1	**SSIP**	**SSIP**	**SSIP**	**SSIP**	**SSIP**	**SSIP**	**SSIP**	**SSIP**	**CIP-A1**	**SSIP**	**SSIP**	**SSIP**
EC	**SSIP**	**SSIP**	**SSIP**	**SSIP**	**SSIP**	**SSIP**	**SSIP**	**SSIP**	**CIP-A2**	**CIP-A2**	**SSIP**	**SSIP**

Table 1. Solvation Structure predicted by AIMD from initial SSIP solvation model.

	Anions											
	Fluorinated Alkoxy Anions								Other Anions			
	Borates			Aluminates								
Solvents	B(TFIP)$_4$	B(HFIP)$_4$	B(PIN)$_2$	Al(TFIP)$_4$	Al(HFIP)$_4$	Al(TFTB)$_4$	Al(HFTB)$_4$	Al(PFTB)$_4$	TFSI	PF$_6$	CB$_{11}$H$_{12}$	BPh$_4$
G1	CIP-A1	CIP-A1	CIP-A1	CIP-A1	CIP-A1	CIP-A1	CIP-A1	CIP-A1	CIP-A1	CIP-A2	SSIP	SSIP
EC	CIP-A1	CIP-A1	CIP-A1	CIP-A1	CIP-A1	CIP-A1	CIP-A1	CIP-A1	CIP-A1	CIP-A2	SSIP	SSIP

Table 2. Solvation Structure predicted by AIMD from initial CIP-A1 solvation model.

	Anions											
	Fluorinated Alkoxy Anions								Other Anions			
	Borates			Aluminates								
Solvents	B(TFIP)$_4$	B(HFIP)$_4$	B(PIN)$_2$	Al(TFIP)$_4$	Al(HFIP)$_4$	Al(TFTB)$_4$	Al(HFTB)$_4$	Al(PFTB)$_4$	TFSI	PF$_6$	CB$_{11}$H$_{12}$	BPh$_4$
G1	CIP-A2	CIP-A2	CIP-A2	CIP-A2	CIP-A2	CIP-A2	CIP-A2	CIP-A2	CIP-A2	CIP-A2	SSIP	SSIP
EC	CIP-A2	CIP-A2	CIP-A2	CIP-A2	CIP-A2	CIP-A2	CIP-A2	CIP-A2	CIP-A2	CIP-A2	SSIP	SSIP

Table 3. Solvation Structure predicted by AIMD from initial CIP-A2 solvation model.

Next, we describe several examples of Ca battery electrolytes from AIMD simulations. **Figures 2a-2c** show snapshots of Ca[Al(TFIP)$_4$]$_2$ with G1 solvents in SSIP, CIP-A1, and CIP-A2 structures at 10 ps of AIMD simulations. It turns out that the solvation structure was mostly maintained until the end of 10 ps. This result was consistent across other Ca battery electrolytes with fluorinated alkoxy anions, such as B(TFIP)$_4^-$, B(HFIP)$_4^-$, B(PIN)$_2^-$, Al(HFIP)$_4^-$, Al(TFTB)$_4^-$, Al(HFTB)$_4^-$, and Al(PFTB)$_4^-$. In an EC solvation environment (**Figures 2d-2f**), the solvation trend was consistent with the results in the G1 environment, except for the coordination number around the Ca cation.

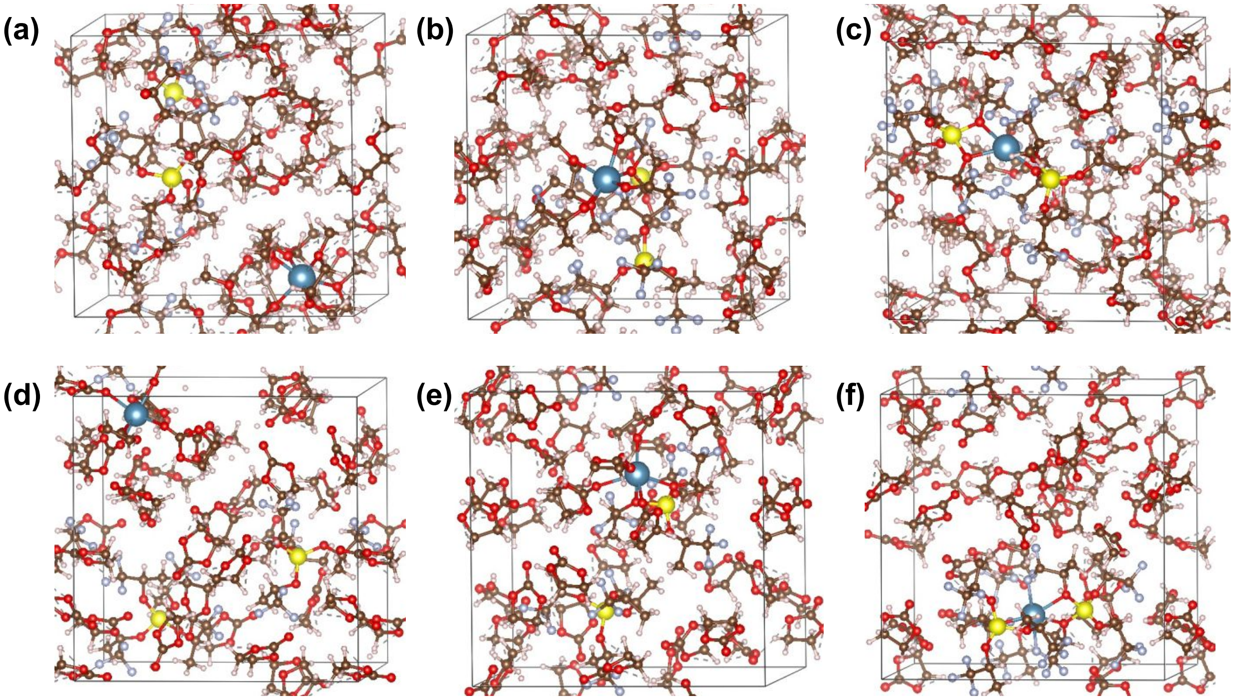

Figure 2. Electrolytes of 0.5 M Ca[Al(TFIP)$_4$]$_2$ in the presence of solvent species with a density of 1 g/ml. (a)-(c) present the snapshots for the final structure of SSIP, CIP-A1, and CIP-A2 in G1 solvent species after AIMD simulations. (d)-(f) present the snapshots for the final structure of SSIP, CIP-A1, and CIP-A2 in EC solvent species after AIMD simulations. In the snapshots, the colors assigned to the atoms: red for O, brown for C, white for H, blue for Ca, yellow for Al, and light blue for F.

In contrast, other types of electrolytes with TFSI$^-$, PF$_6^-$, CB$_{11}$H$_{12}^-$, and BPh$_4^-$ anions exhibited variations in solvation structure during AIMD simulations. **Figures 3a-3c** illustrate snapshots of Ca[TFSI]$_2$ with G1 solvents at 10 ps. When the Ca cation is initially solvated by G1 solvents (SSIP), CIP-A1 was formed. However, in the case of CIP-A1 and CIP-A2, the initial solvation structure was maintained until the end of the AIMD simulations. This solvation behavior was consistently observed in the EC solvent condition (**Figures 3d-3f**). For PF$_6^-$ (**Figure S2**), due to the compact size of PF$_6^-$, the anion appears to have relatively more flexibility and diffuse easily. The Ca cation forms CIP-A2 in both G1 and EC environments overall. However, only the initial SSIP structure in the G1 solvent retained its SSIP configuration. For CB$_{11}$H$_{12}^-$ (**Figure S3**) and BPh$_4^-$ (**Figure S4**), the hydrogen bonds in the outer shell of the anions prevented the Ca cation from coordinating directly with the anions, though it remained in close proximity. This limited the cation's freedom to change its structure due to the bulky nature of the anions. Therefore, solvation may not be likely to occur in the presence of these anions.

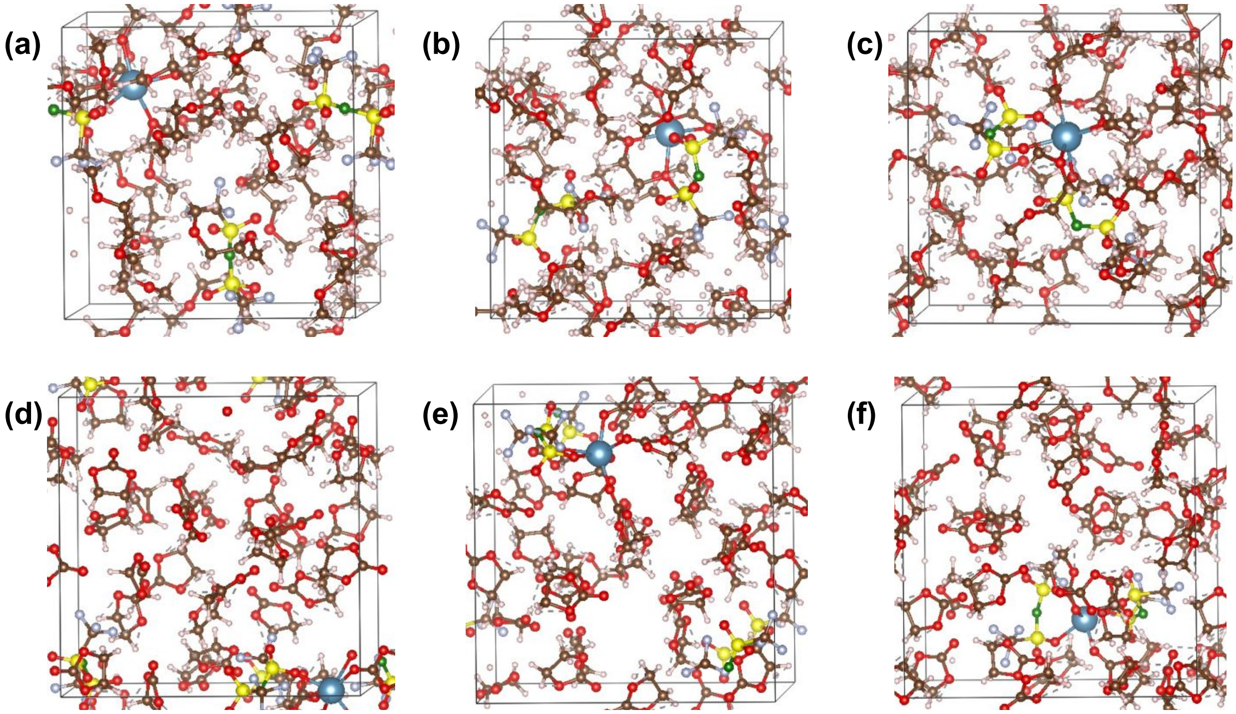

Figure 3. Electrolytes of 0.5 M Ca[TFSI]$_2$ in the presence of solvent species with a density of 1 g/ml. (a)-(c) present the snapshots for the final structure of SSIP, CIP-A1, and CIP-A2 in G1 solvent species after AIMD simulations. (d)-(f) present the snapshots for the final structure of SSIP, CIP-A1, and CIP-A2 in EC solvent species after AIMD simulations. In the snapshots, the colors assigned to the atoms: red for O, brown for C, white for H, blue for Ca, yellow for S, green for N, and light blue for F.

AIMD simulations show that Ca salt can dissociate from the initial structure, but decomposition species were not observed in any cases. To confirm the relationship between decomposition and charge transfer, we conducted Bader charge analysis.[38,39] This is supported by the observation that transferred charges between species are negligible. **Figure S5** shows the transferred charges in the example of 0.5 M Ca[Al(TFIP)$_4$]$_2$ in G1 solvents.

2. Frontier Orbitals

In this section, we present the frontier orbitals of Ca battery electrolytes, including the HOMO and LUMO levels, using the last ten AIMD trajectories. In our previous study, the frontier orbitals for CIP-A2 solvation structure were considered in an implicit solvent environment. There, we demonstrated that higher reductive stability was observed when the anion was less fluorinated, and oxidative stability increased when the anion was more fluorinated.[13] In this study, we investigated the frontier orbitals with the explicit inclusion of G1 solvent in first solvation shell. As noted in the AIMD section, most initial solvation structures were maintained in the Ca battery electrolyte with fluorinated alkoxy anions, but not in others. Therefore, we present the results using four different solvation environments: explicit models of CIP-A1, CIP-A2, and SSIP, and an implicit model of CIP-A2. [13] However, some electrolyte species showed few solvation structures due to changes after AIMD simulations.

We note the distinctions between explicit and implicit solvent models. As shown in **Figure 4**, the order of magnitude in both HOMO and LUMO levels varies depending on the model used, with trends in anion behavior showing slight differences between the two conditions (data colored in red and yellow). However, the implicit model still follows a similar qualitative trend. This suggests that while both approaches offer valuable insights and are qualitatively comparable, explicit models provide greater accuracy for solvated electrolyte conditions, making them essential for precise simulations, despite the higher computational costs.

In the explicit model, we investigated the effect of fluorination in alkoxy anions. First, the effect of fluorination in boron-centered alkoxy anions, such as $B(TFIP)_4^-$ and $B(HFIP)_4^-$, did not exhibit a clear trend within the same solvation structure. For example, in the $B(HFIP)_4^-$ anion, the order of the LUMO level depending on the structure does not match the order of the HOMO level. In contrast, fluorinated aluminum-centered anions, such as $Al(TFIP)_4^-$, $Al(HFIP)_4^-$, $Al(TFTB)_4^-$, $Al(HFTB)_4^-$, and $Al(PFTB)_4^-$, exhibited a trend in which more fluorination decreases both LUMO and HOMO levels. This suggests that boron and aluminum may induce different effects on frontier orbitals in these fluorinated alkoxy anions. Second, the degree of deviation of the HOMO and LUMO levels for CIP-A1, CIP-A2, and SSIP varied according to the type of anions. Even within the same type of anion, the distribution of HOMO and LUMO levels depends on the solvation structure. For example, the $B(TFIP)_4^-$ anion shows that the HOMO level was relatively more distributed than the LUMO level. Third, the order of reductive and oxidative stability was predicted. Overall, less fluorination exhibits a higher LUMO, indicating higher reductive stability of the electrolyte. In contrast, more fluorination shows a lower HOMO, indicating higher oxidative stability. In particular, the lowest HOMO level was observed in the Al(PFTB)$_4^-$ anion, showing the highest oxidative stability. The highest LUMO level was observed in the B(PIN)$_2^-$ anion, indicating the highest reductive stability.

We then compared the stability of Ca battery electrolytes with other anions. The electrolyte with the B(Ph)$_4^-$ anion might have poor oxidative and reductive stability based on the relatively higher HOMO and lower LUMO levels. Other electrolytes with anions such as $CB_{11}H_{12}^-$, PF_6^-, and TFSI$^-$ exhibit better stability and have a similar order in both LUMO and HOMO levels. In comparison to this reference, CIP-A1 of B(HFIP)$_4^-$, CIP-A2 of Al(HFIP)$_4^-$, CIP-A2 of Al(HFTB)$_4^-$, and CIP-A1 and CIP-A2 of Al(PFTB)$_4^-$ show lower HOMO levels. CIP-A2 of B(HFIP)$_4^-$, CIP-A1 and SSIP of B(PIN)$_2^-$, and CIP-A2 of Al(TFIP)$_4^-$, CIP-A2 of Al(TFTB)$_4^-$, and CIP-A2 of Al(HFTB)$_4^-$ present higher LUMO levels. As a result, we identified that the Ca battery electrolyte with the Al(HFTB)$_4^-$ anion in CIP-A2 structure will be oxidatively and reductively stable based on the lower HOMO and a higher LUMO level. However, it should be considered whether the Ca battery electrolyte with the Al(HFTB)$_4^-$ anion prefers CIP-A2 over other solvation structure (CIP-A1 and SSIP). We will address this in the next section.

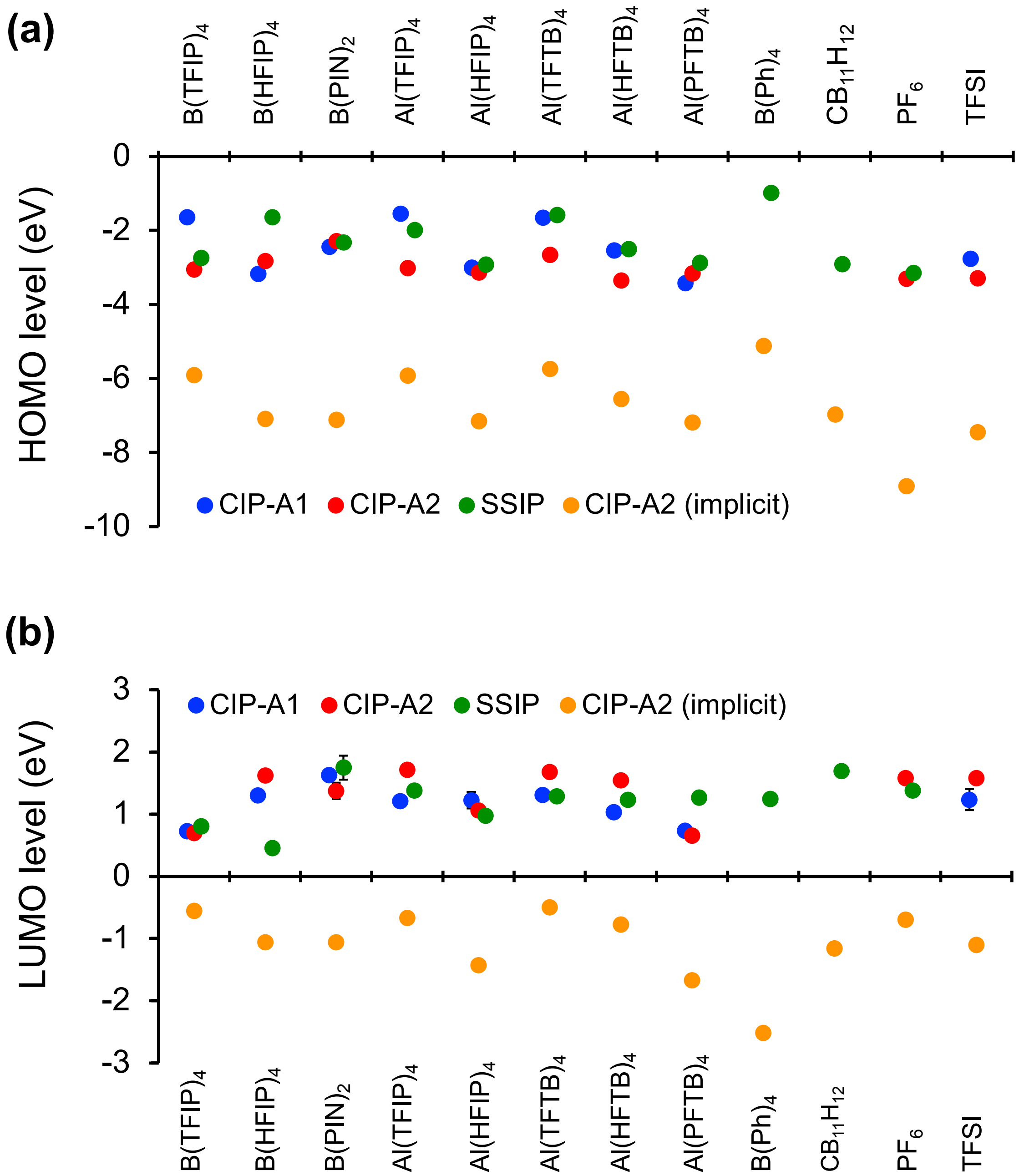

Figure 4. (a) HOMO and (b) LUMO levels for the Ca battery electrolytes under explicit and implicit G1 solvent condition. In the explicit condition, the HOMO and LUMO level were obtained using the average of the last ten AIMD trajectories before the end of the AIMD simulation (10 ps). The error bars represent the standard deviation of the last ten trajectories. Three explicit models are presented: CIP-A1 (colored blue), CIP-A2 (colored red), and SSIP (colored green).

Additionally, one implicit model is included (colored yellow). The data for the implicit solvent condition were referenced from our previous study.[13]

3. Solvation Structure Predicted from Formation Free Energy Calculations

Figure 5 demonstrates the favorability of solvation structure with different anions and G1 solvents. In the heatmap plot, the red color (indicating positive ΔG) suggests a preference for the left-side species, while the blue color (indicating negative ΔG) suggests a preference for the right-side species. Dark colors represent a strong preference, whereas light colors indicate a weaker preference. We investigated the favorability of structure between 'CIP-A2 vs. SSIP', 'CIP-A1 vs. SSIP', and 'CIP-A1 vs. CIP-A2' within similar types of anion groups, as well as the effect of the number of solvents on SSIP formation.

Both Ca fluorinated alkoxyborates and Ca fluorinated alkoxyaluminates in G1 solvents illustrate that the SSIP state is favorable, particularly when the anion ligand contains more fluorine atoms. This finding also corresponds with previous experimental comparisons between $Al(HFIP)_4^-$ and $Al(TFTB)_4^-$ anions.[24] In the case of the $TFSI^-$ anion, CIP is favorable, while other anions (PF_6^-, $CB_{11}H_{12}^-$, and BPh_4^-) show a weak preference between SSIP and CIPs (CIP-A1 and CIP-A2). When comparing CIP-A1 and CIP-A2 structures, **Figure 5c** reveals that the transformation energy difference between the two species is less than 0.1 eV. This indicates that most anions may easily transition between the CIPs, and their overall preference is weak. In the analysis of the number of solvents, a smaller number of solvents was favorable for forming SSIP, whereas a higher number of solvents favored the formation of either CIP-A1 or CIP-A2. This shows that the cost of solvation energy increases with the increase in solvent coordination number

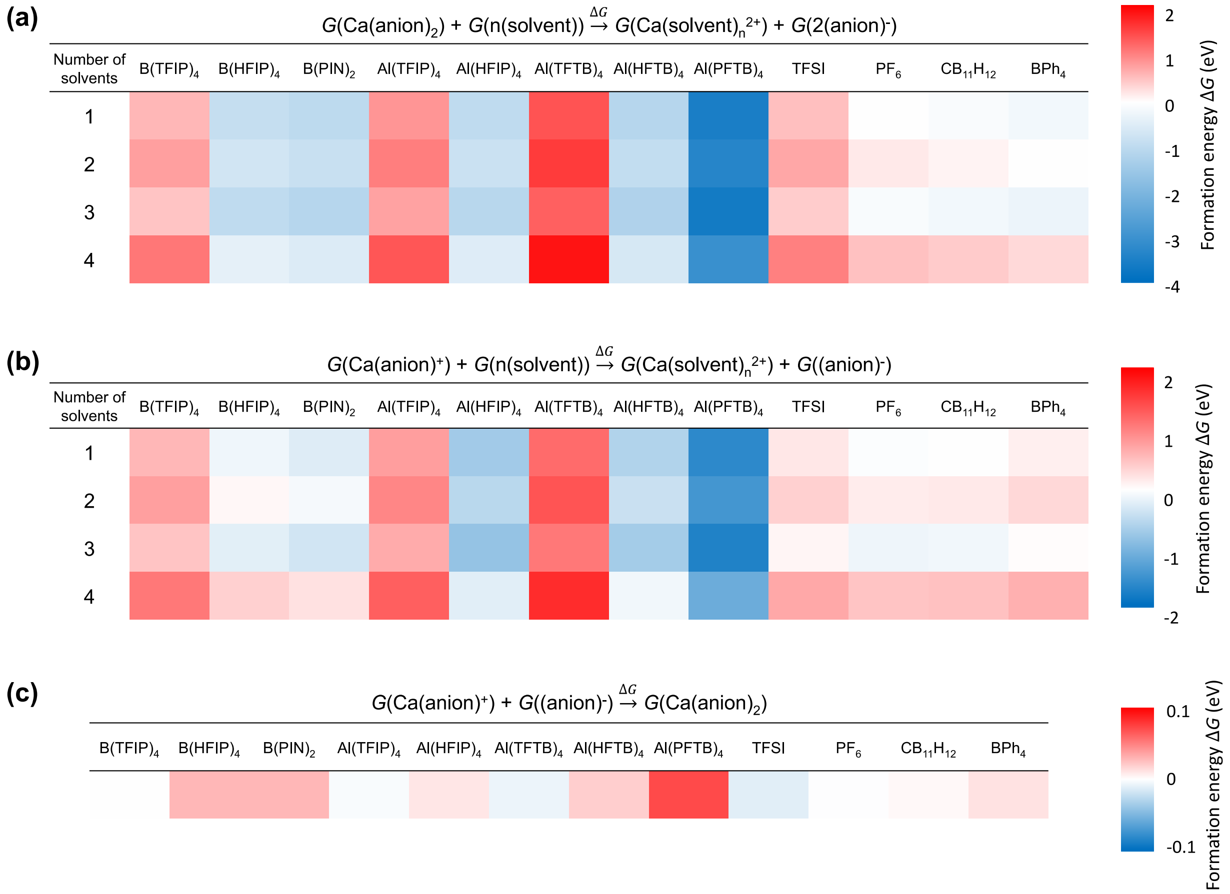

Figure 5. Heat map illustrating the formation free energies (ΔG) among electrolyte solvation structures with G1 solvents: (a) SSIP formation energy transformation from CIP-A2, (b) SSIP formation energy transformation from CIP-A1, and (c) CIP-A2 formation energy transformation from CIP-A1.

Figure S6 demonstrates the preference of solvation structure with G2 solvents. The trend observed for alkoxyborates and alkoxyaluminates remains similar to that with G1 solvents. However, for other anions, the preference for solvation structure is mostly weak. This is attributed to the change in solvation structure. G2 is longer than G1 and allows for only one or two solvent molecules to chelate the Ca cation, whereas four G1 molecules can coordinate with the Ca cation. This coordination effect on metal and ligand was also studied elsewhere, not only in Ca [14] but also in Mg [40] batteries.

Figure 6 displays the favorability of solvation structure with EC solvents. Overall, the heat map shows more dramatic transformations between SSIP and CIPs in **Figures 6a and 6b**. A smaller number of solvents is favorable for forming SSIP, while a higher number of solvents favors either CIP-A1 or CIP-A2. In alkoxyborates and alkoxyaluminates, the SSIP state is strongly favored, as seen in $B(HFIP)_4^-$, $B(PIN)_2^-$, $Al(HFTB)_4^-$, and $Al(PFTB)_4^-$, when compared to CIP-A2 states. However, most of these change their solvation structure and prefer the CIP-A1 state relative to SSIP, except for $Al(PFTB)_4^-$, which still prefers to form SSIP. The other anions ($TFSI^-$, PF_6^-, $CB_{11}H_{12}^-$, and BPh_4^-) follow a similar trend to the alkoxyborates and alkoxyaluminates. When comparing structure between CIP-A1 and CIP-A2, most of these anions prefer CIP-A1. However, the energy difference is still less than 0.1 eV, indicating a weak preference.

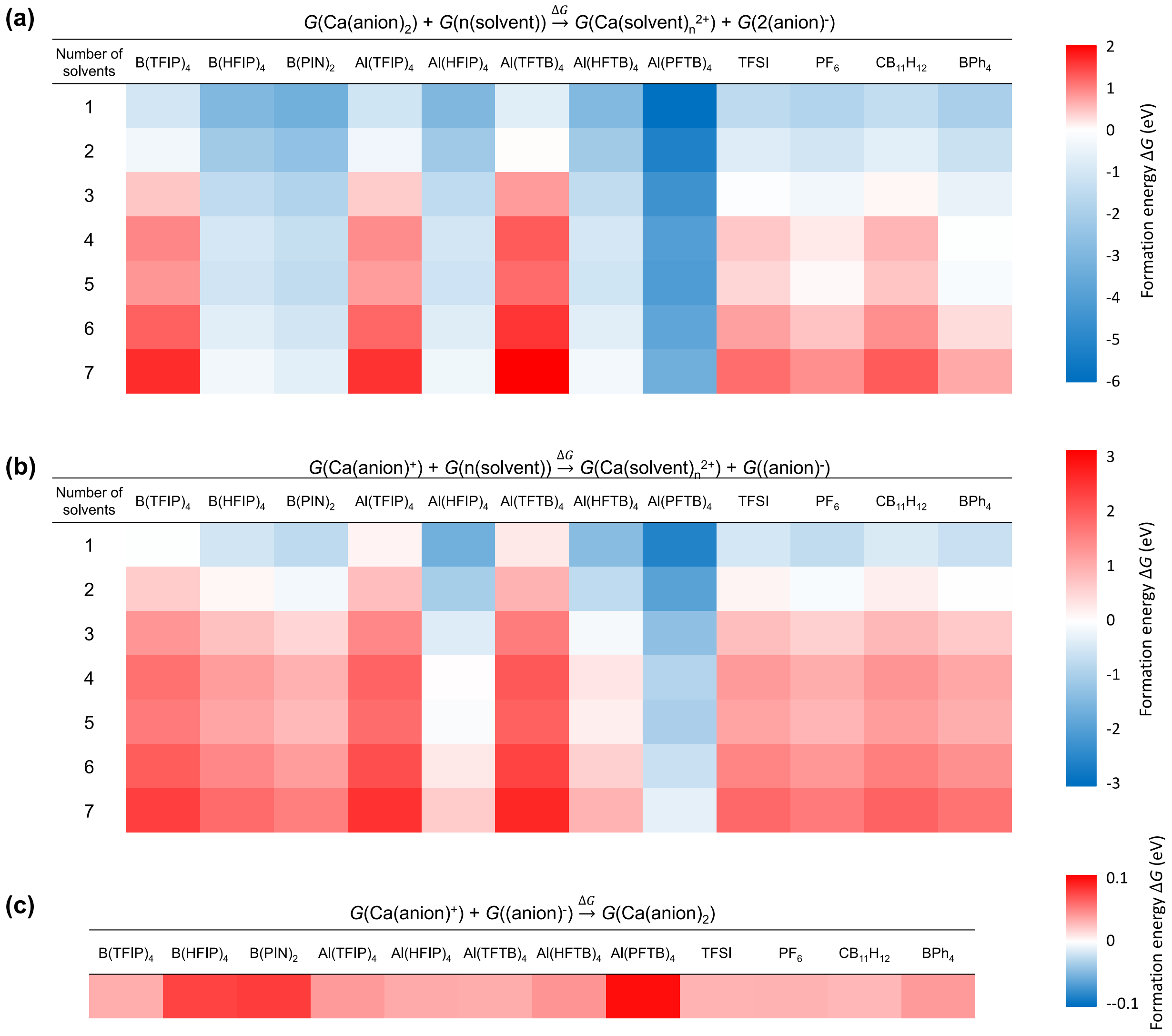

Figure 6. Heat map illustrating the formation free energies (ΔG) among electrolyte solvation structures with EC solvents: (a) SSIP formation energy transformation from CIP-A2, (b) SSIP formation energy transformation from CIP-A1, and (c) CIP-A2 formation energy transformation from CIP-A1.

Figure S7 illustrates the favorability of solvation structure with THF solvents. Overall, the heat map shows a clear preference for $Al(PFTB)_4^-$ and $TFSI^-$ in **Figure S7**. **Figure S7a** shows that most alkoxyborates, alkoxyaluminates, and other anions with Ca cation prefer to form CIP-A2 relative to SSIP, whereas $Al(PFTB)_4^-$ strongly prefers SSIP formation. $B(PIN)_2^-$ shows a slight preference for SSIP. **Figure S7b** presents that both $Al(PFTB)_4^-$ and $TFSI^-$ prefer SSIP compared to CIP-A1, while other anions prefer to form CIP-A1. When comparing the structure between CIP-A1 and CIP-A2, the energy difference is less than 0.1 eV in most cases, indicating a weak preference. Exceptionally, $Al(PFTB)_4^-$ and $TFSI^-$ show a distinct preference. Overall, considering all heat maps, SSIP is the preferable solvation structure with $Al(PFTB)_4^-$, while CIP-A2 is preferable with the $TFSI^-$ anion in THF solvent conditions.

4. Solvation Structure Predicted from Machine Learning Force Fields

Figure 7 compares the atomic forces and energies between the first-principles calculations and the MLFF predictions for all the configurations in the training data. As shown in **Figure 7**, the MLFF predictions closely align with the first-principles calculations, exhibiting no obvious bias between the training and predicted data. The Root Mean Squared Error (RMSE) for the energy and force are 9.63E-4 eV/atom and 6.06E-2 eV/Å, respectively, with coefficients of determination (R^2) of 0.935 and 0.993 for the energy and force, respectively. Both the RMSE and R^2 values indicate that the MLFF has accurately fitted the first-principles calculations. After validating the force field, the MLFF was used to perform MD simulations of 0.5 M $Ca(TFSI)_2$:G1.

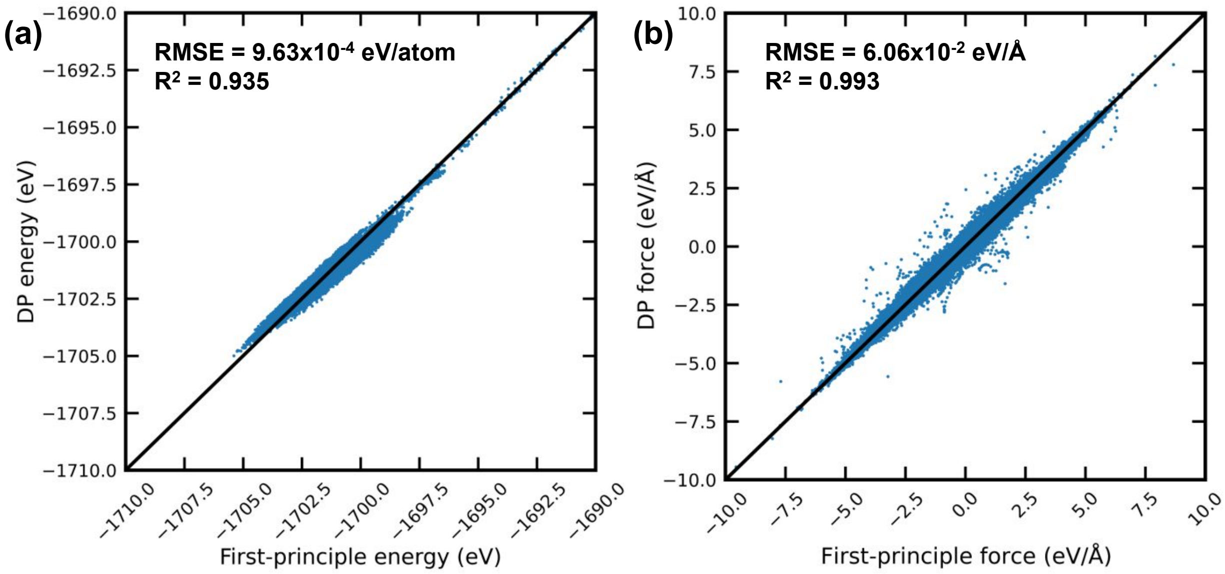

Figure 7. Comparison between the first-principles (FP) calculations and the MLFF (referred as DPGEN (DP) predicted results: (a) potential energy obtained from first-principles (FP) calculations vs. the predicted potential energy by DP, (b) atomic force obtained from FP calculations vs. the predicted potential energy by DP. All the configurations are included.

Figure 8d displays the final structures of the MD simulations using the SSIP structure as the initial configuration (**Figure 8a**). As discussed in the methods section, parallel simulations were conducted for CIP-A1, CIP-A2, and SSIP as initial configurations. The figures demonstrating the configuration changes for CIP-A1 and CIP-A2, along with their initial structures, are shown in **Figures 8b and 8c**. In all MD simulations with MLFF, the major evolution of the configurations occurred before 0.5 ns, after which the configurations remained stable for the remainder of the simulations. It was observed that all trajectories transitioned to the CIP-A1 structure by the end of the simulations (**Figures 8d-8f**), regardless of their initial structures (**Figures 8a-8c**). This indicates that the CIP-A1 structure is the most stable configuration for 0.5 M Ca(TFSI)$_2$:G1.

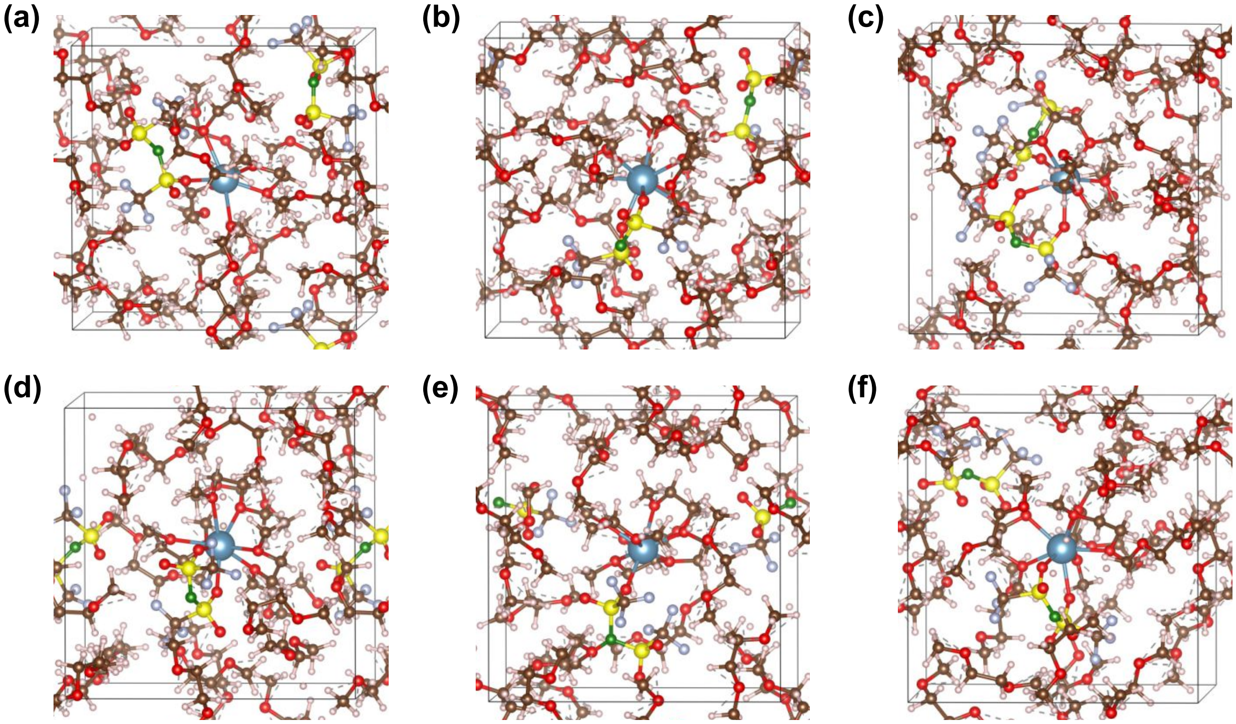

Figure 8. The initial structure and relaxed structure of the 0.5 M Ca[TFSI]$_2$ in the G1 solvents, simulated with the MLFF. (a)-(c) presents the initial structure of the SSIP, CIP-A1, and CIP-A2 structure. (d)-(f) displays the final relaxed structure after performing MD simulations with the MLFF. In the snapshots, the colors assigned to the atoms: red for O, brown for C, white for H, blue for Ca, yellow for S, green for N, and light blue for F.

Discussion

The MLFF offers a valuable solution to overcome the timescale limitations of AIMD simulations, significantly aiding in the exploration of the configurational space of battery electrolytes. However, the current MLFF has some drawbacks. An accurate and reliable MLFF requires a large amount of training data, which adds significant time and computational cost to collect or generate. While the active learning procedure implemented in DPGEN has automated the data collection process, the time and computational cost associated with the iterations remain substantial. Additionally, the cutoffs for the iterations and the amount of data required for the MLFF are arbitrary. In this work, advancing the timescale limitation was our primary goal, while the length scale of the simulations was not a major concern. However, achieving simulations on a greater timescale and length scale will require even more data.

To accurately predict the solvation structures of 0.5 M $Ca(TFSI)_2$:G1, we combined various computational methods, including AIMD, formation free energy calculation, and MLFF. The summary indicates that CIP-A1 may be the most stable solvation structure. The AIMD simulations demonstrate that either CIP-A1 or CIP-A2 can be observed, depending on the initial solvation structure. The formation free energy calculations show that both CIP-A1 and CIP-A2 have lower formation energies than SSIP, and the free energy difference between CIP-A1 and CIP-A2 is less than 0.1 eV. Thus, both CIP-A1 and CIP-A2 are possible, consistent with the AIMD results. Lastly, the MLFF also predicts a preference for CIP-A1, confirming the results from the AIMD and formation free energy calculation.

Overall, the three different approaches consistently predict that the Ca cation is partially solvated (CIP-A1). We did not impose any biased molecular structures for the starting structures, nor did we anticipate any specific predicted result. However, the different computational results converged on a consistent and harmonious outcome.

These findings align with a Raman experiment, which demonstrated that a fragment of CIPs exhibits a much higher ratio of 80% compared to others.[10] Additionally, the authors reported that the Ca battery electrolyte of 0.5 M $Ca(TFSI)_2$:G2 showed a much higher SSIP ratio than 0.5 M $Ca(TFSI)_2$:G1. This study also presents that SSIP was more favorable than CIP (CIP-A1 and CIP-A2) in G2 (**Figure S6**) compared to G1 (**Figure 5**) based on heat map analysis. This supports the reliability of the free energy analysis since it matches well with the experimental observations.

The solvating power can change with different solvents. [41] In this study, our heat map analysis shows that solvating power may vary due to the solvent species and its coordination number (CN) with the Ca cation. For G1, EC, and THF, a higher CN favored CIP formation, whereas for G2, a higher CN favored SSIP formation.

Here is an example involving the Ca cation and $B(TFIP)_4^-$ anion: For G1, CIP was favorable regardless of the change in CN. For G2, CIP was still favorable with one G2 solvent, but the free energy difference was negligibly small for two G2 solvents, indicating a shift in favorability toward SSIP. For EC, SSIP was favorable with one solvent, whereas CIP became more stable with 2 to 7 solvents. There was a transition between one and two solvents for less fluorinated alkoxy anions ($B(TFIP)_4^-$, $Al(TFIP)_4^-$, and $Al(TFTB)_4^-$). For more highly fluorinated alkoxy anions, SSIP remained stable. For THF, CIP was always favorable with the $B(TFIP)_4^-$ anion, and CN did not affect the transition between CIP and SSIP within the same anion.

For other anions, including $TFSI^-$, PF_6^-, $CB_{11}H_{12}^-$, and $B(Ph_4)^-$, the trend differed from alkoxy anions. $TFSI^-$ showed that CIP was favorable in G1, G2, and THF regardless of the number of solvents. For EC, there was a transition between CIP and SSIP: SSIP was favorable with one solvent, but CIP became more favorable with 2 to 7 solvents. PF_6^- showed that SSIP and CIP could coexist due to a weak dependence on the solvation structure in G1. For G2, SSIP was more favorable. For EC, SSIP was favorable with two solvents, then CIP became favorable with 3 to 7 solvents. For THF, CIP was favorable. $CB_{11}H_{12}^-$ showed that SSIP and CIP could coexist due to a weak dependence on the solvation structure in G1. SSIP was favorable in G2. In EC, SSIP was favorable with one solvent, and CIP became favorable with 2 to 7 solvents. In THF, SSIP was favorable with 1 to 5 solvents, and CIP was favorable with 6 solvents. $B(Ph_4)^-$ showed that SSIP and CIP could coexist in G1. SSIP was favorable in G2. In EC, SSIP was favorable with 1 to 2 solvents, whereas CIP was favorable with 3 to 7 solvents. CIP was favorable in THF.

The donor number (DN) indicates the ability of a solvent to solvate the Ca cation.[11] The donor numbers of G1, G2, EC, and THF are 20, 18, 16.4, and 20, respectively. [42] We found a correlation between DN and solvation structure. Solvents with lower DN (G2 and EC) exhibited more dramatic changes in solvation structure within the same anion, whereas solvents with higher DN (G1 and THF) showed consistency in solvation structure. This trend varied for each anion. In most cases, a higher number of solvents around the Ca cation became unfavorable compared to CIP formation, likely due to the higher formation energy required for higher coordination numbers. Fluorination in alkoxy anions also affected the solvating power, leading to different solvation structures. This was reported in an experimental study involving the Ca cation and $TFSI^-$ anion. [10] In addition, Zeng et al. reported that low DN solvents are preferentially desolvated at the electrolyte/cathode interface. [43]

The solvating power and structure also affect electrolyte stability during metal electrodeposition. A strongly solvated Ca cation may require higher activation energy for decoordination, leading to a larger overpotential.[14] For Ca alkoxy aluminate electrolytes, cyclic voltammetry (CV) revealed that $Ca[Al(HFIP)_4]_2$ in G2 solvent exhibits superior Ca plating and stripping performance compared to $Ca[Al(TFTB)_4]_2$ in G2. Electrospray ionization mass spectrometry (ESI-MS) observations indicated that $Ca[Al(HFIP)_4]_2$ in G2 prefers the formation of SSIP, while $Ca[Al(TFTB)_4]_2$ in G2 favors CIP,[24] which is also confirmed in this work (Figure S6). A similar trend was observed in G1 solvent, likely due to the structural similarity between G1 and G2. However, this trend differs in solvents with cyclic structures, such as ethylene carbonate (EC) and tetrahydrofuran (THF). Figure 2 illustrates the case of EC, where $Al(HFIP)_4^-$ tends to favor SSIP, whereas $Al(TFTB)_4^-$ may transition between SSIP and CIP depending on the solvent environment. In contrast, the behavior in THF (Figure S7) shows both $Al(TFTB)_4^-$ and $Al(HFIP)_4^-$ anions generally favor CIP, although $Al(HFIP)_4^-$ demonstrates a stronger preference for SSIP compared to $Al(TFTB)_4^-$.

Overall, based on this work and existing experimental literature, Ca electrolytes that favor SSIP are expected to exhibit superior electrochemical performance. Although the reductive and oxidative stabilities, as indicated by the HOMO and LUMO levels, reflect the electrochemical stability of the electrolyte, achieving a balance between structure stability and efficient stripping and plating will be crucial for defining effective electrolyte design guidelines.

In addition, from the perspective of electrode, electrochemical performance remains a critical factor. Favorable solvation structures and CN may change as the electrolyte approaches the electrode. [44,45] Particularly, Ca electrolytes with alkoxy anions may require additional computational studies to elucidate how cation-anion interaction strengths and their distance from the electrolyte/electrode interface are correlated.

Conclusion

In this study, we investigated favorability of solvation structure and identified a trend of solvation preferences based on the number of molecular species, such as anions and solvents. We used multiple computational approaches (AIMD simulations; DFT calculation and the heat map analysis for the formation free energy in the first solvation shell; and MLFF) converged to provide a similar prediction in solvation structure, as shown in $Ca(TFSI)_2$:G1 electrolyte. This provides evidence of accuracy of the generated MLFF embedded in MD simulations, and the ab initio prediction for both DFT and AIMD is still meaningful though they have some limits in the application. Based on our findings, the comprehensive solvation study may require multiple approaches that complement each other perspectives. These cumulative findings will provide insights for designing novel battery electrolytes, not only for Ca electrolytes but also for a broader range of battery electrolyte.

Supplementary Information

Supplementary Figures (Figures S1-S7): Introduction of solvents with anions that make up the Ca battery electrolyte species; Electrolytes of 0.5 M $Ca[PF_6]_2$ in the presence of solvent species with a density of 1 g/ml; Electrolytes of 0.5 M $Ca[CB_{11}H_{12}]_2$ in the presence of solvent species with a density of 1 g/ml; Electrolytes of 0.5 M $Ca[BPh_4]_2$ in the presence of solvent species with a density of 1 g/ml; Bader charge analysis for electrolytes of 0.5 M $Ca[Al(TFIP)_4]_2$ with a density of 1 g/ml; Heat map illustrating the formation energies (ΔG) among electrolyte solvation structures with G2 solvents; Heat map illustrating the formation energies (ΔG) among electrolyte solvation structures with THF solvents.

Author Contributions

Heonjae Jeong and Haimeng Wang contributed equally. Heonjae Jeong: conceptualization, data curation, formal analysis, investigation, visualization, methodology, supervision, writing - original draft, writing - review & editing. Haimeng Wang: data curation, formal analysis, investigation, writing - original draft, writing - review & editing. Lei Cheng: funding acquisition, supervision, writing - review & editing.

Notes

The authors declare no competing financial interest.

Acknowledgements

This research was supported by the Joint Center for Energy Storage Research (JCESR), a U.S. Department of Energy, Energy Innovation Hub. The submitted manuscript has been created by UChicago Argonne, LLC, Operator of Argonne National Laboratory (“Argonne”). Argonne, a U.S. Department of Energy Office of Science laboratory, is operated under contract no. DE-AC02-06CH11357. We gratefully acknowledge use of the Bebop or Swing or Blues cluster in the Laboratory Computing Resource Center at Argonne National Laboratory.

ORCID ID

Heonjae Jeong: https://orcid.org/0000-0003-4452-049X
Haimeng Wang: https://orcid.org/0000-0001-8006-0932
Lei Cheng: https://orcid.org/0000-0002-3902-1680

References

1 R. J. Gummow, G. Vamvounis, M. B. Kannan and Y. He, *Advanced Materials*, 2018, **30**, 1801702.

2 A. Ponrouch, C. Frontera, F. Bardé and M. R. Palacín, *Nat Mater*, 2016, **15**, 169–172.

3 D. Wang, X. Gao, Y. Chen, L. Jin, C. Kuss and P. G. Bruce, *Nat Mater*, 2018, **17**, 16–20.

4 Z. Li, O. Fuhr, M. Fichtner and Z. Zhao-Karger, *Energy Environ Sci*, 2019, **12**, 3496–3501.

5 R. B. Araujo, V. Thangavel and P. Johansson, *Energy Storage Mater*, 2021, **39**, 89–95.

6 J. Young and M. Smeu, *Adv Theory Simul*, 2021, **4**, 2100018.

7 S. S. R. K. C. Yamijala, H. Kwon, J. Guo and B. M. Wong, *ACS Appl Mater Interfaces*, 2021, **13**, 13114–13122.

8 M. Shakourian-Fard, G. Kamath, S. M. Taimoory and J. F. Trant, *The Journal of Physical Chemistry C*, 2019, **123**, 15885–15896.

9 K. Kisu, S. Kim, T. Shinohara, K. Zhao, A. Züttel and S. Orimo, *Sci Rep*, 2021, **11**, 7563.

10 N. T. Hahn, D. M. Driscoll, Z. Yu, G. E. Sterbinsky, L. Cheng, M. Balasubramanian and K. R. Zavadil, *ACS Appl Energy Mater*, 2020, **3**, 8437–8447.

11 J. D. Forero-Saboya, E. Marchante, R. B. Araujo, D. Monti, P. Johansson and A. Ponrouch, *The Journal of Physical Chemistry C*, 2019, **123**, 29524–29532.

12 A. Ponrouch, J. Bitenc, R. Dominko, N. Lindahl, P. Johansson and M. R. Palacín, *Energy Storage Mater*, 2019, **20**, 253–262.

13 H. Jeong, E. P. Kamphaus, P. C. Redfern, N. T. Hahn, N. J. Leon, C. Liao and L. Cheng, *ACS Appl Mater Interfaces*, 2023, **15**, 6933–6941.

14 L. H. B. Nguyen and J.-S. Filhol, *Adv Energy Mater*, 2023, **13**, 2300311.

15 J. Young, P. M. Kulick, T. R. Juran and M. Smeu, *ACS Appl Energy Mater*, 2019, **2**, 1676–1684.

16 A. M. Melemed, A. Khurram and B. M. Gallant, *Batter Supercaps*, 2020, **3**, 570–580.

17 T. Yang, T.-C. Ma, X.-J. Ye, X.-H. Zheng, R. Jia, X.-H. Yan and C.-S. Liu, *Physical Chemistry Chemical Physics*, 2024, **26**, 4589–4596.

18 Y. Yi, Y. Xing, H. Wang, Z. Zeng, Z. Sun, R. Li, H. Lin, Y. Ma, X. Pu, M. M.-J. Li, K.-Y. Park and Z.-L. Xu, *Angewandte Chemie International Edition*, 2024, **63**, e202317177.

19 J. Young and M. Smeu, *Adv Theory Simul*, 2021, **4**, 2100018.

20 A. T. Landers, J. Self, S. A. McClary, K. J. Fritzsching, K. A. Persson, N. T. Hahn and K. R. Zavadil, *The Journal of Physical Chemistry C*, 2023, **127**, 23664–23674.

21 A. M. Melemed, D. A. Skiba, K. J. Steinberg, K.-H. Kim and B. M. Gallant, *The Journal of Physical Chemistry C*, 2023, **127**, 19886–19899.

22 H. Song, Y. Li, F. Tian and C. Wang, *Adv Funct Mater*, 2022, **32**, 2200004.

23 A. Shyamsunder, L. E. Blanc, A. Assoud and L. F. Nazar, *ACS Energy Lett*, 2019, **4**, 2271–2276.

24 N. J. Leon, S. Ilic, X. Xie, H. Jeong, Z. Yang, B. Wang, E. W. C. Spotte-Smith, C. Stern, N. Hahn, K. Zavadil, L. Cheng, K. A. Persson, J. G. Connell and C. Liao, *J Phys Chem Lett*, 2024, **15**, 5096–5102.

25 J. Self, N. T. Hahn, K. D. Fong, S. A. McClary, K. R. Zavadil and K. A. Persson, *J Phys Chem Lett*, 2020, **11**, 2046–2052.

26 L. Martínez, R. Andrade, E. G. Birgin and J. M. Martínez, *J Comput Chem*, 2009, **30**, 2157–2164.

27 M. Frisch, G. W. Trucks, H. B. Schlegel, G. E. Scuseria, M. A. Robb, J. R. Cheeseman, G. Scalmani, V. Barone, B. Mennucci and G. A. Petersson, *Inc., Wallingford CT*, 2009, **121**, 150–166.

28 A. D. Becke, *J Chem Phys*, 1992, **96**, 2155–2160.

29 P. J. Stephens, F. J. Devlin, C. F. Chabalowski and M. J. Frisch, *J Phys Chem*, 1994, **98**, 11623–11627.

30 C. Lee, W. Yang and R. G. Parr, *Phys Rev B*, 1988, **37**, 785.

31 G. Kresse and J. Furthmüller, *Comput Mater Sci*, 1996, **6**, 15–50.

32 G. Kresse and J. Furthmüller, *Phys Rev B*, 1996, **54**, 11169.

33 J. P. Perdew, K. Burke and M. Ernzerhof, *Phys Rev Lett*, 1996, **77**, 3865.

34 G. Kresse and D. Joubert, *Phys Rev B*, 1999, **59**, 1758.

35 H. Wang, L. Zhang, J. Han and E. Weinan, *Comput Phys Commun*, 2018, **228**, 178–184.

36 Y. Zhang, H. Wang, W. Chen, J. Zeng, L. Zhang, H. Wang and E. Weinan, *Comput Phys Commun*, 2020, **253**, 107206.

37 A. P. Thompson, H. M. Aktulga, R. Berger, D. S. Bolintineanu, W. M. Brown, P. S. Crozier, P. J. In't Veld, A. Kohlmeyer, S. G. Moore and T. D. Nguyen, *Comput Phys Commun*, 2022, **271**, 108171.

38 G. Henkelman, A. Arnaldsson and H. Jónsson, *Comput Mater Sci*, 2006, **36**, 354–360.

39 W. Tang, E. Sanville and G. Henkelman, *Journal of Physics: Condensed Matter*, 2009, **21**, 084204.

40 P. Jankowski, J. M. G. Lastra and T. Vegge, *Batter Supercaps*, 2020, **3**, 1350–1359.

41 C.-C. Su, M. He, R. Amine, T. Rojas, L. Cheng, A. T. Ngo and K. Amine, *Energy Environ Sci*, 2019, **12**, 1249–1254.

42 V. Gutmann, *Coord Chem Rev*, 1976, **18**, 225–255.

43 F. Zeng, S. Li, S. Hu, M. Qiu, G. Zhang, M. Li, C. Chang, H. Wang, M. Xu, L. Zheng, Y. Tang, C. Han and H.-M. Cheng, *Adv Funct Mater*, 2024, **34**, 2302397.

44 A. Baskin and D. Prendergast, *The Journal of Physical Chemistry C*, 2016, **120**, 3583–3594.

45 J. G. Connell, M. Zorko, G. Agarwal, M. Yang, C. Liao, R. S. Assary, D. Strmcnik and N. M. Markovic, *ACS Appl Mater Interfaces*, 2020, **12**, 36137–36147.

All data is presented in the main text and the ESI.